NUCLEAR
INSTRUMENTS
& METHODS
IN PHYSICS
RESEARCH
Section A

Initial measurements of the UCLA rf photoinjector *

S.C. Hartman [a],[**], N. Barov [a], C. Pellegrini [a], S. Park [a], J. Rosenzweig [a], G. Travish [a],
R. Zhang [a], C. Clayton [b], P. Davis [b], M. Everett [b], C. Joshi [b], G. Hairapetian [b]

[a] *Department of Physics, University of California, Los Angeles, CA 90024, USA*
[b] *Electrical Engineering Department, University of California, Los Angeles, CA 90024, USA*

The 1.5 cell standing wave rf photoinjector has been operated for the past several months using a copper cathode. The photoinjector drive laser produces sub 2 ps pulses of UV ($\lambda = 266$ nm) light with up to 200 μJ/pulse which generates up to 3 nC of charge. The emittance of the photoinjector was measured as a function of charge, rf launching phase, and peak accelerating field. Also, the quantum efficiency and pulse lengths of the laser beam and the electron beam were measured.

1. Introduction

We report the initial results of the operation of the UCLA 4.5 MeV photocathode rf gun [1–3]. This electron source is part of a 20 MeV compact electron linac described before. It will be used for studies of the interaction of relativistic beams, plasmas, and the generation of coherent radiation. All the components of this system have been built and tested. Full assembly will be completed during the fall of 1993. Our initial work has been dedicated to a characterization of the photocathode rf gun, which is the electron source for the system. As part of this work we have measured the electron beam emittance and the quantum efficiency of a copper cathode under different conditions. We will summarize the overall performance of the gun and our plans for future development. The photocathode rf gun has also been used to study a thin plasma lens. This experiment demonstrated electron beam focusing and confirmed theoretical expectations.

2. Accelerator system description

2.1. Rf system

The gun is powered by a SLAC XK5 type klystron producing 24 MW of rf power with a pulse duration of 4 μs. The rf system is driven by a signal produced by a master oscillator clock at a frequency of 38.08 MHz.

This signal is multiplied 75 times to produce the klystron operating frequency of 2.856 GHz and is then sent to a 1 kW solid state amplifier. The amplifier signal in turn feeds the klystron. This ensures the timing and a feed back loop stabilizes the laser pulse to rf jitter to less than 4 ps.

2.2. Rf photoinjector

The photocathode rf gun is based on the Brookhaven design. It consists of a one and a half cell standing wave accelerator producing a beam with an energy up to 4.5 MeV. Accelerating gradients of up to 100 MV/m are achieved.

2.3. Laser system

For single photon photoemission, the photon energy must exceed the work function of Cu (4.65 eV). The photoinjector drive laser was designed to produce < 2 ps laser pulses at 266 nm (4.66 eV) [4] with up to 200 μJ/pulse. This is accomplished using chirped pulse amplification and compression of a mode-locked YAG laser ($\lambda = 1.064$ μm) and frequency upconverting using two KD*P doubling crystals. The drive laser is a mode locked Nd-YAG oscillator cavity. To compress the pulse the laser is matched into a 500 m fiber to produce a frequency chirp. The chirped pulse is then amplified a million times by a regenerative amplifier and sent to a grating pair where it is compressed. Once it leaves the compression stage the laser beam is frequency upconverted to green by a KD*P crystal. Then it is doubled again to UV, 266 nm, by a second frequency doubling crystal. The upconversion efficiency is typically 10%.
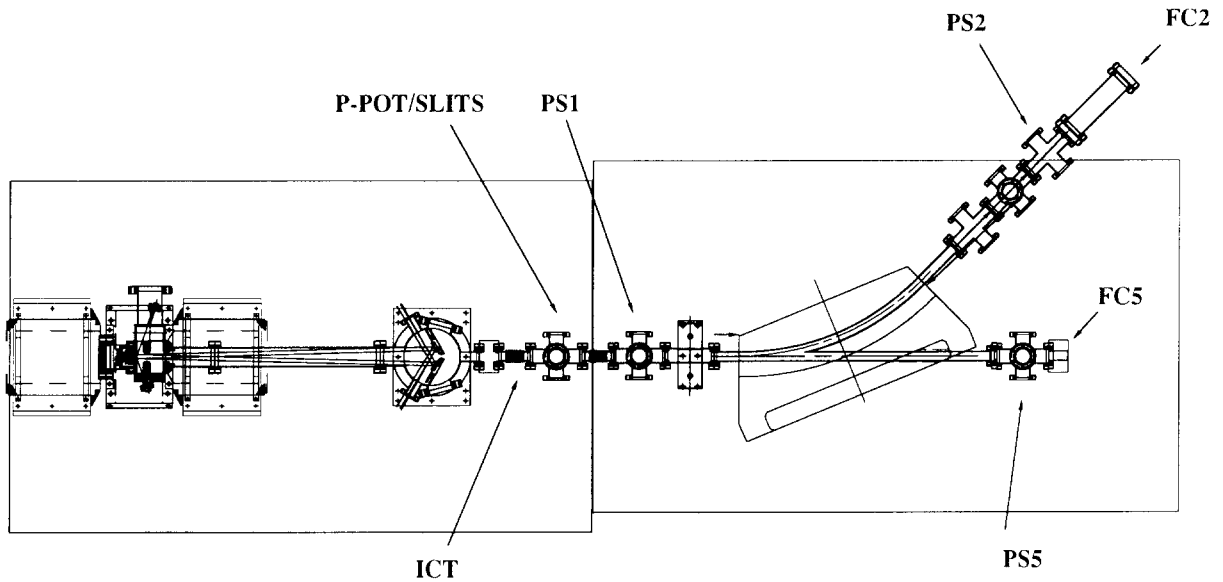
Fig. 1. Beamline configuration.

2.4. Diagnostics

The electron beam diagnostics are as follows. The main diagnostics are the phosphor screens which monitor the spot size. An integrating current transformer, ICT, is used to measure the electron beam charge along with Faraday cups at various locations. Some of the phosphor screens are floated so that they can double as Faraday cups. A dipole is used to measure the energy and energy spread of the beam (Fig. 1).

3. Electron beam energy and energy spread

3.1. Rf induced jitter

The time jitter of the laser pulse and the fluctuations in the rf voltage are of deep concern for future FEL experiments. In order to get a measure of the rf induced pulse-to-pulse jitter we measured the fluctuations in the peak dark current electrons. Fig. 2 shows a plot of $\delta p/p$ (%) versus shot number and has a $\sigma = 0.067\%$.

3.2. Timing jitter

In Fig. 3 we show the jitter in peak momentum of the photoelectrons; this gives a measure of not only the rf jitter but also the jitter between the laser and the rf. One can see that the resulting rms momentum fluctuation is 0.25% and is due mainly to the residual laser pulse jitter.
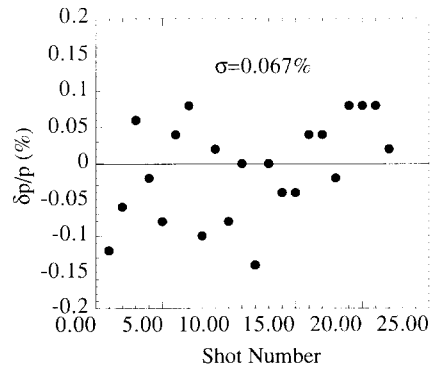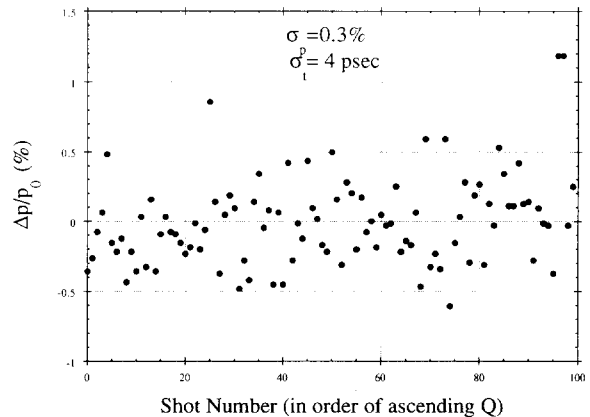

Fig. 2. $\delta p/p$ versus shot number ($\sigma = 0.067\%$).

Fig. 3. Jitter in peak momentum of the photoelectrons.

We measured the dependence of the beam energy versus rf phase to calibrate the absolute phase, Fig. 7. This dependence shows that the accelerating field in the two cells is unbalanced with a larger field in the full cell. Introducing an imbalance of 50 MV/m in the half cell and 100 MV/m in the full cell the data can be fit using the analytical theory of Kim [5]. From the beam energy measurements we can also determine the gun shunt impedance which is evaluated to be 36 MΩ/m; this is smaller than the value expected from the Superfish calculations. The beam energy spread measured at low current, 50 pC, is less than 0.2%. However, due to the large space charge effects it increases rapidly with charge, when using the damaged cathode. The space charge growth was modeled with PARMELA [6] and is discussed later in section 7.

4. Emittance measurements

The UCLA photoinjector [7] produces a very high peak current beam, up to 250 A, at relatively low energy, 4.5 MeV. The consequence of this is that electron beam transport is in the highly non-linear space charge dominated regime. Since the beam is space charge dominated, linear beam transport for-

malisms such as matrix transformations do not apply. This means that the usual quadrupole scan technique is not valid for the UCLA photo-electron beam. To overcome this problem a pepper pot emittance measurement apparatus has been designed and implemented. The pepper pot is designed such that upon the electron beams passage through the pepper pot it is transformed from a space charge dominated beam to an emittance dominated beam. Once the electron beam is in the emittance dominated regime one can use linear transform theory to calculate the emittance. Because of pulse-to-pulse fluctuations in the beam charge the measurement must be made single shot. All the beam parameters are measured every shot via fast sample and hold electronics.

4.1. Pepper pot considerations

The pepper pot used in these experiments is actually an array of eight slits. After the electron beam traverses the slits it drifts approximately 20 cm onto a phosphor screen. The image then gives the full phase space, emittance, and other beam parameters. The width of the slit was chosen by considering the envelope equation, Eq. (1). For a round beam, A is the normalized beam transverse dimension, β is the nor-
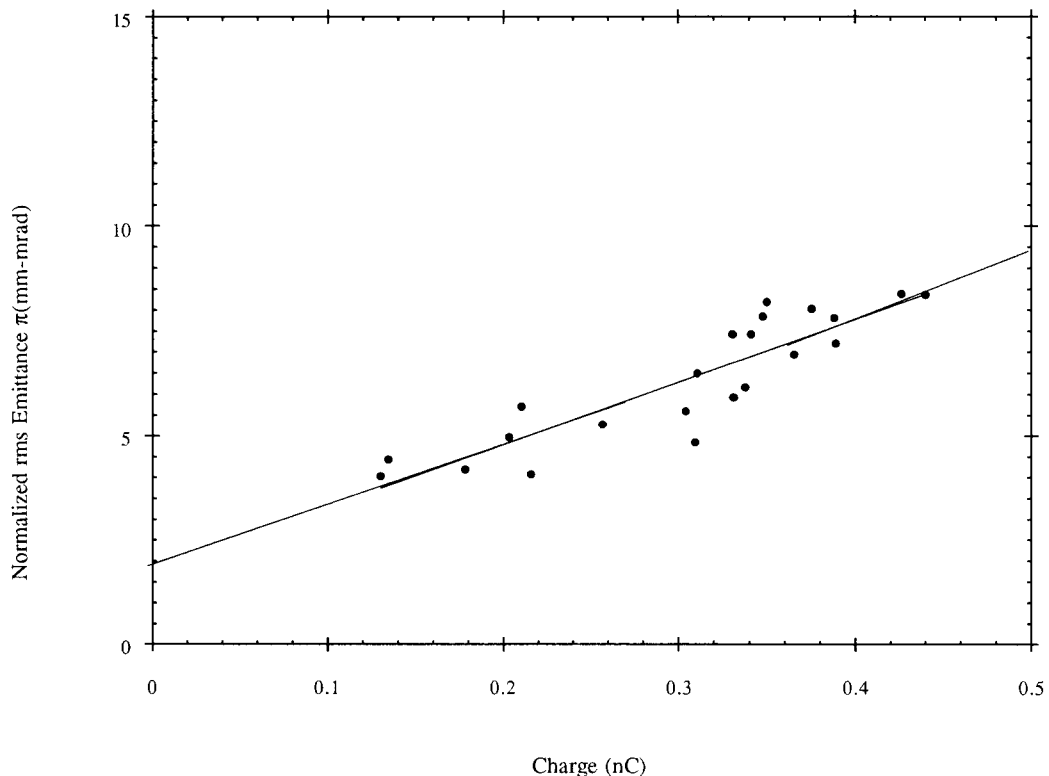

Fig. 4. Emittance versus charge.

malized velocity, γ is the normalized energy, and ϵ is the normalized emittance

$$A'' - \frac{\beta\gamma k}{A} - \frac{\epsilon_n^2}{A^3} = 0 \quad \text{where} \quad A = a[\beta\gamma]^{1/2}.$$

(1)

Taking the ratio of the space charge to emittance term yields,

$$\mathscr{R} = \frac{2a^2 I_p}{(\beta\gamma)^{1/2}\epsilon_n^2 I_A},$$

(2)

where I_p is the peak electron beam current and I_A is the Alfven current of 17 kA. When this ratio is greater than unity, space charge forces dominate the electron beam and when the ratio is less than unity emittance effects dominate the electron beam transport. By choosing the slit widths wisely we can go from the space charge dominated regime to the emittance dominated regime. Now if we scale the transverse dimension by η,

$$I_p' = \eta^2 I_p; \quad a' = \eta a; \quad \epsilon_n' = \eta\epsilon_n,$$

(3)

the ratio of the space charge term to the emittance term becomes

$$\mathscr{R}' = \mathscr{R}\eta^2.$$

(4)

Using this expression and plugging in the numbers for the UCLA experiment we get $\eta = 0.01$ which corresponds to a slit size of 50 μm.

4.2. Definition of emittance

Electron beams do not typically have sharp boundaries so the definition of emittance is ambiguous at times. Some laboratories define emittance for a certain percentage of the beam particles enclosed within an ellipse, commonly 63% or 90% [8]. For the following measurements we define our emittance as the root-mean-square emittance [8] given by

$$\epsilon_{rms} = \left(\langle x^2\rangle\langle x'^2\rangle - \langle x\cdot x'\rangle^2\right)^{1/2},$$

(5)

and the normalized emittance is given by

$$\epsilon_n = \beta\gamma\epsilon_{rms}.$$

(6)

4.3. Emittance vs charge

The electron beam emittance in all of the following was done with a beam momentum of 3.5 MeV/c. The first step in measuring the emittance is to measure the linear increase as a function of charge. The laser energy delivered to the cathode was varied and the emittance was measured as a function of charge transported through the ICT and to the slits. For all other
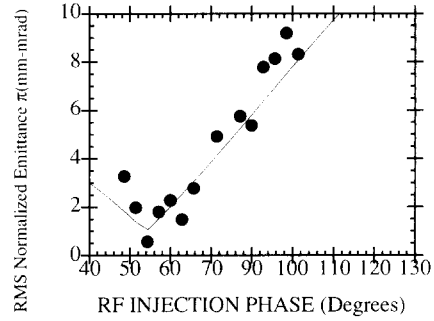

Fig. 5. Zero intercepts of rf injection phases.

parameters fixed one expects the emittance to be linear in charge as in the following equation [5]

$$\epsilon_x^{sc} = \frac{\pi}{4}\frac{1}{\alpha\kappa}\frac{1}{\sin(\vartheta_0)}\frac{I}{I_A}\mu.$$

(7)

Each emittance versus charge plot takes approximately 30–60 s to complete, Fig. 4. So one can adjust on-line the beam parameters to minimize the electron beam emittance. This is a very powerful diagnostic.

4.4. Rf induced emittance vs laser injection phase

To measure the rf induced emittance versus laser injection phase many emittance versus charge data runs were taken with different laser injection phases. The procedure for extracting the rf induced emittance is as follows. For each laser injection phase the data is plotted and fit to a line. The slope and intercept of this line are then extracted. The zero charge intercept gives the rf induced emittance. Fig. 5 is a plot of the zero intercepts of rf injection phases. The data is then fit to the equation

$$\epsilon_x^{rf} = \alpha\kappa\langle x^2\rangle\sqrt{\langle(\Delta\phi)^2\rangle}\,|\cos\langle\phi\rangle|.$$

(8)

Notice that the data have the correct scaling as one would expect.

4.5. Emittance vs peak accelerating field

To explore the effect of the variation of the peak electric field the rf power into the photoinjector was varied, Fig. 6. Since the final beam energy is proportional to the peak accelerating field we recover the expected linear decreasing of the emittance.

4.6. Rf injection phase calibration

The beam energy versus rf injection phase was measured in order to calibrate the absolute phase, Fig. 7. The equations of motion were then integrated and compared to the experiment. This data highlights the
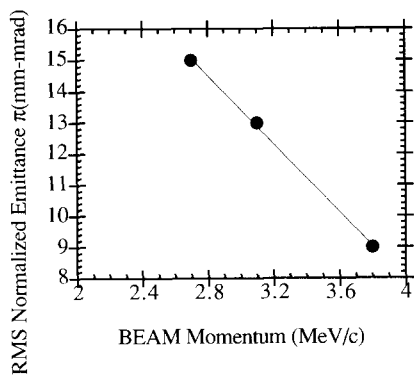
Fig. 6. Effect of variation of peak electric field.

Fig. 8. Gun balance measurement.

fact that the rf gun was unbalanced. The field in the full cell was 1.8 times that in the half cell, Fig. 8. This was confirmed with a bead pull experiment after the gun was removed for a postmortem cold test.

The emittance measurements presented above are the first round results and suffer from a few problems. The first is that upon installation of the photoinjector the micrometer which holds the cathode in place was bumped. This caused the gun to become detained. The gun was then retuned on-line by adjusting the cathode position until the shunt impedance was maximized. Since the shunt impedance of the full cell is larger than the half cell the peak fields in the full cell were favored. The second artificial emittance growth mechanism was that the phosphor screens which were used to measure the spots were at 45° angles with respect to the beam. This enlarged the spot size artificially and due to short depth of focus induced some parallax broadening and blurring of the image. These problems were eliminated in a subsequent attempt to re-measure the emittance but due to time limitations the measurements were not completed in time for this conference.
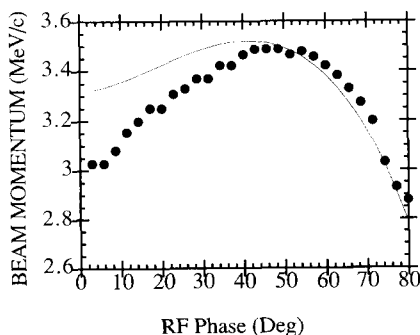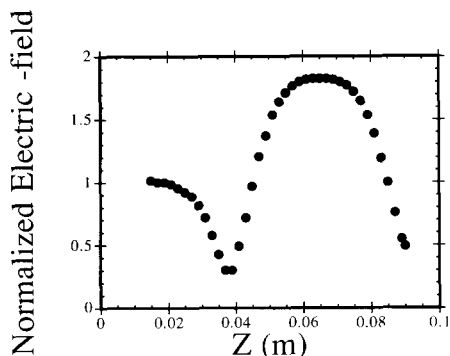

Fig. 7. Beam energy versus rf injection phase.

The emittance values given are thus a set of worse case values.

5. Pulse length measurements

5.1. Experimental setup

A 250 μm thick fused silica etalon [9] served as the Cerenkov radiator. The etalon side where the electron beam entered was sanded forming a diffuse surface to prevent bunch lengthening due to multiple reflections. Furthermore, the beam entrance side of the etalon was covered with a 0.005 in. thick aluminum foil which provides grounding of the Cerenkov radiator and prevents any scattered laser light from entering the field of view of the Cerenkov light. The etalon was attached on a mount which was externally rotatable about an axis perpendicular to the beam. For a relativistic electron beam, the angle of Cerenkov radiation with respect to the beam axis is

$$\theta_c = \cos^{-1}\left(\frac{1}{n}\right), \tag{9}$$

where n is the index of refraction of the medium. For fused silica $n = 1.46$ and therefore $\theta_c = 47°$. The Cerenkov radiator setup is depicted in Fig. 9.

This Cerenkov radiator allows 1 ps time resolution. The limiting factor in the bunch length measurements is the streak camera. We use a Hadland Imacon 500 streak camera. At the fastest sweep speed of 20 ps/mm, the time resolution is no better than 3.5 ps. The streak camera cannot be installed directly viewing the Cerenkov detector because of the high levels of radiation inside the lead shielding. Therefore, the Cerenkov light is transported through a maze in the lead shielding. Because the light intensity levels are near the detection limits of the streak camera, the Cerenkov image is reduced by a factor of 4 when focused on the streak camera slit. To achieve 3.5 ps resolution, a 25

μm slit is used at the entrance to the streak camera. Accounting for the 400% reduction in image size, the 25 μm slit infers a 100 μm acceptance at the Cerenkov radiator. The maximum time delay possible between any two Cerenkov photons created by an infinitely small thin electron beam is 1 ps. When combined with the resolution of the streak camera, the overall resolution of the Cerenkov streak system is 3.6 ps. The streak camera resolution was verified by streaking the laser pulses. This steak camera cathode is sensitive to green 532 nm light but not to UV 266 nm light. Therefore, the laser pulses were streaked after the first doubling crystal. A $\sqrt{2}$ reduction in pulse width should occur when the green light is doubled to UV. In streaking short pulses, care is taken to avoid space charge saturation within the streak camera which can result in erroneous measurements. Fig. 10 depicts a typical laser streak and its corresponding integrated intensity plot.

5.2. Streak measurements

The laser pulse streak resulted in a pulse width of 3.9 ps FWHM. Since the resolution of the streak camera is 3.5 ps, the actual laser pulse width is 1.7 ps. Auto correlation measurements of the cw mode-locked YAG laser beam result in pulse widths of 2 ps FWHM. After doubling to green light, the pulse width is expected to decrease by $\sqrt{2}$, producing 1.4 ps pulses in reasonable agreement with the streak camera measure-
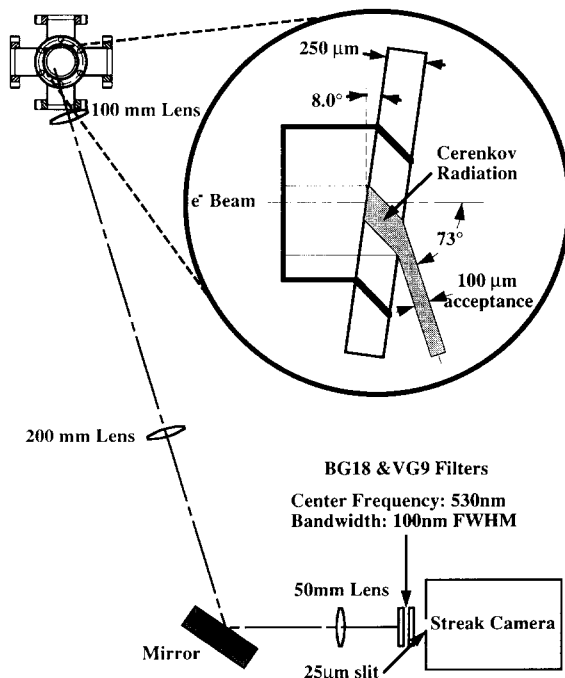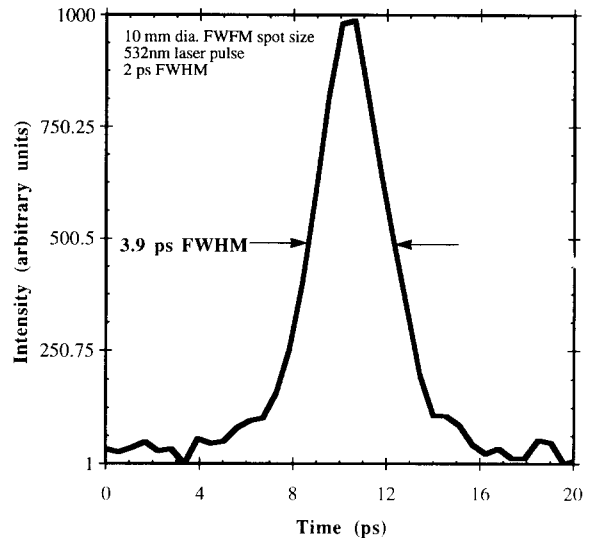

Fig. 10. A typical laser streak and its corresponding integrated intensity plot.

ments. The streak images appear spotted due to the low light levels incident on the streak camera. Low light levels are required to avoid space charge lengthening in the streak camera and to achieve 3.5 ps resolution. In analyzing Cerenkov streaks, the images are integrated along the space axis to provide better statistics. Each array element corresponds to 0.56 ps. Since the Cerenkov streak system resolution is 3.6 ps, a smoothing algorithm is used to average over the six nearest neighbors in the integrated array. The first streak measurements were taken with 70° laser injection. Laser injection at 70° produces bunch lengthening from a time delay across the cathode as the laser wavefront strikes it. This produces an electron beam with a linear space time correlation. This correlation is present in the Cerenkov streak shown in Fig. 11. A laser spot size of 2 mm produces a time delay of

$$\tau \approx \frac{2 \text{ mm}}{c \, \cos(70°)} \approx 20 \text{ ps.} \qquad (10)$$

The measured delay from the streak in Fig. 11 was 25 ps. When the streak is corrected for the delay across the wavefront, the measured pulse width becomes 13 ps. At 2° injection, the time delay across the cathode is insignificant and the Cerenkov streaks indicate the electron bunch length directly. By focusing the laser spot to 2 mm, we were able to move the laser spot to an undamaged portion of the cathode. A streak from the undamaged cathode is depicted in Fig. 12. Streaks from the damaged portion of the cathode resulted in slightly longer bunches due to an elongated tail. Bunch length measurements with the Cerenkov radiator and streak camera resulted in 9–15 ps FWHM for various
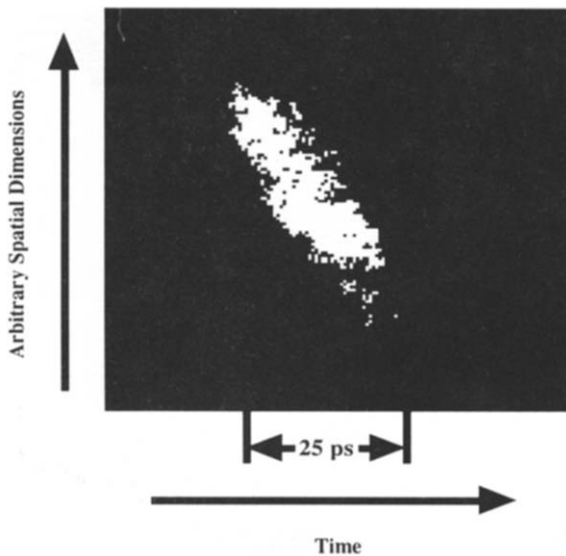

Fig. 9. Cerenkov radiator setup.

Fig. 11. Cerenkov streak showing linear space time correlation.

Fig. 13. Laser injection geometry.

charge levels from 0.2 to 2.6 nC, however no correlation was found between the bunch length and the charge output from the rf gun.

All the streak camera measurements indicate electron bunch lengths longer than 8 ps. Measurements for 2° incidence on the undamaged portion of the cathode provide the shortest bunch length measurements averaging 12 ps. However, the 2° measurements from damaged parts of the cathode clearly characterize longer bunches with more time structure and long tails. These measurements contradict the assumption that electron bunches will mimic the laser pulses in time. One source
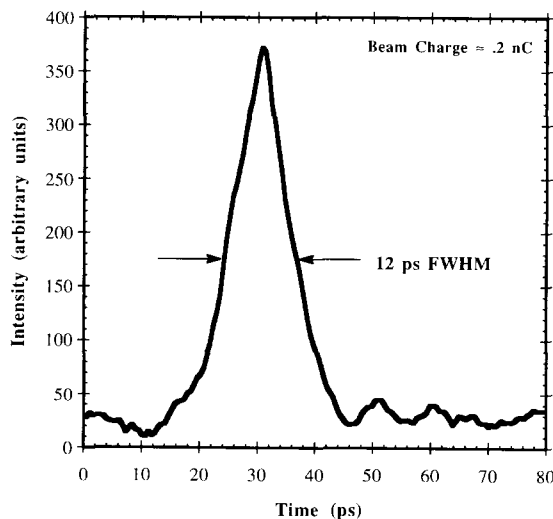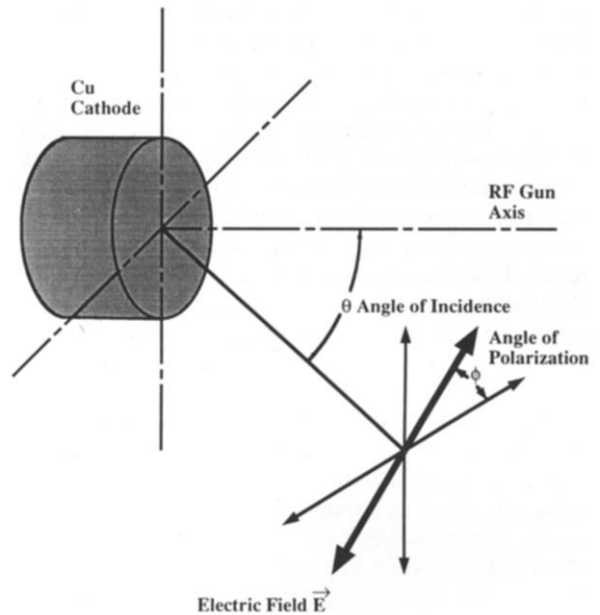
for bunch lengthening is space charge. The quantum efficiency data indicated significant reductions in charge production due to space charge. Microemitters can further aggravate this problem, possibly accounting for pulse lengthening and time structure of the streaks from damaged portions of the cathode. PARMELA [10] simulations were performed for various output bunch charge levels from 100 pC to 1.3 nC. These simulations show a bunch lengthening as output charge is increased. For typical charge levels between 0.4 and 1.0 nC PARMELA predicts bunch lengths from 9 to 15 ps. These bunch lengths predictions are within the scatter of the measured bunch lengths, however the measurements did not indicate a correlation with charge level.

6. Quantum efficiency

6.1. Laser geometry

The laser injection geometry [11] is shown in Fig. 13. The polarization angle ϕ is the angle the electric field makes with respect to the plane of incidence. Therefore, 0° corresponds to p-polarized light and 90° corresponds to s-polarized light. A 1/2 waveplate allows continuous rotation of the laser polarization through a full 360°. The angle θ is the angle of incidence of the laser beam with respect to the beam axis of the electron gun. We are limited to only two angles of injection, 70° and 2°.

Fig. 12. Streak from the undamaged cathode.

II. CONTRIBUTIONS

The electron charge is measured with two independent diagnostics, the Faraday cup and the ICT. Both of these diagnostics agree with each other to within 10%. Because the Faraday cup collects significant amounts of dark current, the ICT was used to measure the photo-induced charge per pulse free of the dark current background. A phosphor screen was used to ensure the position of the electron beam was on axis near the center of our diagnostics. The beam energy was measured to be 3.5 MeV using a dipole spectrometer. The Cu cathode received no special surface preparation. After machining, the cathode was installed in the rf gun and baked at 100°C with the gun under vacuum. High power rf conditioning was used to reach a vacuum level of 10^{-9} Torr. During operation of the gun, the laser spot was focused to sub mm spot sizes on the cathode. The high intensity of the laser pulses damaged the cathode surface, further complicating the emission process. The damaged spot is centered on the cathode and therefore all quantum efficiency measurements were made for photoemission from the damaged area.

6.2. Experimental results

Measurements of collected charge vs laser energy for three representative cases are shown in Fig. 14. From these measurements it is clear that saturation of the charge occurs at laser energies above 50 μJ. Therefore, values of quantum efficiency η are taken in the low charge limit. Linear fits for laser energies below 25 μJ are presented and labeled with the quantum effi-
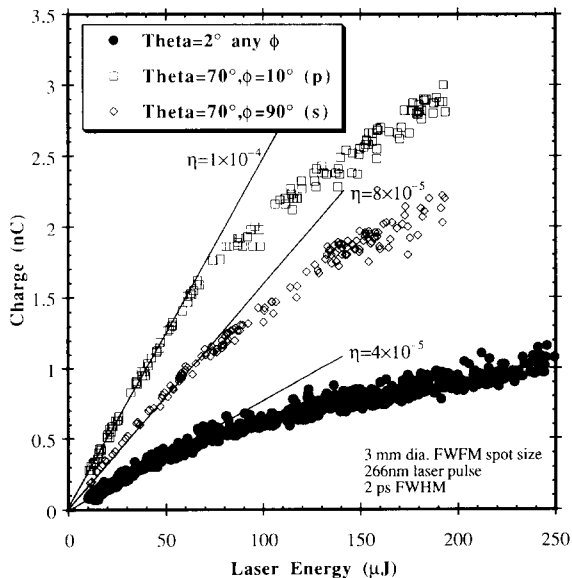

Fig. 15. Polarization dependence of collected charge for a laser energy of 100 μJ.

Fig. 14. Measurements of collected charge versus laser energy for three representative cases.

ciency (η) corresponding to the slope of the line. From these fits, an enhancement in quantum efficiency of 50% is observed for 70° p-polarized over 70° s-polarized light.

Measurements of charge vs laser energy were obtained for various polarization angles. For 2° injection, changing the polarization angle did not affect the charge collected. However, for 70° injection, measurements resulted in curves of similar shape to those of Fig. 3 but which lie in between the 70° s-polarized and 70° p-polarized curves depending on the angle of polarization. Fig. 15 shows the polarization dependence [12] of collected charge for a laser energy of 100 μJ. Identical plots are found at different energies. The functional form of this enhancement fits a $\cos^2\phi$ dependence which implies that the enhancement is dependent on the energy of p-polarized light rather than its electric field.

For laser spot sizes less than 3 mm in diameter, it was possible to inject the laser pulses at 2° incidence without impinging directly on the damaged area of the cathode. Careful quantum efficiency measurements were not taken under these conditions, however a factor of 3 decrease in the quantum efficiency was observed from the undamaged portions of the cathode. Quantum efficiencies of 1×10^{-4} are surprisingly high for photoemission from Cu using 266 nm light (4.66 eV) since the photon energy is very close to the work function of Cu (4.65 eV). The quantum efficiency of Cu has been measured to be 1.5×10^{-5} using 248 [13] nm light and 6×10^{-5} using 193 nm light. Typically the quantum efficiency is higher for light of shorter wavelength. Using the Fowler–Dubridge [14] theory for photoemission, these previous measurements of quan-

tum efficiency can be scaled for our wavelength of 266 nm predicting $\eta \approx 10^{-8}$. The quantum efficiency can be increased in large electric fields (> 10 MV/m) through the Schottky effect. In order to increase η from 10^{-8} to 10^{-4}, electric fields of almost 1 GV/m are necessary at the cathode surface [15]. As was mentioned above, macroscopic fields at the cathode of only 50 MV/m were reached, however in the damaged area electric field enhancement factors of 20 are possible due to the surface roughness. The enhancement of quantum efficiency from the damaged area over undamaged area could explain the factor of 3 decrease in quantum efficiency observed as the laser spot was directed away from the damaged area. A more recent measurement of quantum efficiency (1.4×10^{-4}) for polished, clean Cu with low applied fields using 266 nm laser pulses was reported by Srinivassan-Rao. Although this value agrees with our measurement, it implies that field enhanced emission did not occur and does not explain the difference in photoemission between the damaged and undamaged parts of the cathode. The Fowler–Dubridge theory for the one photon photoelectric effect predicts a linear dependence of charge production on incident laser energy. However, the measured charge vs laser energy manifests a saturation of charge output for laser energies above 50 μJ. The saturation can be explained by space charge effects near the cathode surface. When the electrons are produced by the laser pulse, they are emitted as a thin disk from the cathode: approximately 80 μm thick and 1 mm in diameter corresponding to the laser spot size on the cathode. The space charge electric field between the electron bunch and the cathode can be approximated by a surface charge density and its image charge in the cathode. Using this simple model, a space charge field equaling the accelerating field of 50 MV/m results from only 0.25 nC of charge. This value agrees with the 0° data. The particle accelerator code, PARMELA, has been used to model this space charge effect. This code calculates the space charge forces between a user specified number of test particles as the particles are accelerated from the cathode in an rf gun. However, experimentally the space charge problem is complicated by the cathode damage. Because of this damage, most of the electrons could be produced from microemitters on the cathode surface. At these emitters the space charge could be worse. Despite these limitations in the computer modeling, the PARMELA simulation showed saturation similar to that of experimental data. The increase in quantum efficiency for p-polarized vs s-polarized injection is probably due to the difference in the reflectivity of copper at these polarizations. The reflectivity of a copper mirror was measured as a function of incident angle for both s- and p-polarized 266 nm light. According to the generalized Fowler–Dubridge theory, η is

proportional to absorbed laser energy. A 90% increase in absorption was measured for p-polarized light over s-polarized light, predicting a 90% improvement of the quantum efficiency for p-polarized injection. The measured enhancement was only 50%. This discrepancy could be due to a difference in the relative reflectivities of the damaged cathode in comparison to those of the copper mirror.

7. Simulation of results

One expects the charge measured at the exit of the rf gun to be a linear function of applied laser energy to the photocathode. However, this is not the case for the UCLA experiment thus far. The quantum efficiency data, which measures the total extracted charge out of the rf gun as a function of laser energy, is very non-linear. From zero nC to approximately 0.5 nC the charge extracted follows a linear trend. From 0.5 to 3 nC the extracted charge falls off unexpectedly. In addition, streak camera measurements indicate that the beam's temporal length expands considerably from that of the laser. Because of the highly dynamical behavior of the electron beam near the cathode, a series of PARMELA simulations have been carried out to model the evolution of the beam in this region, both in time structure and in maximum allowed charge. These simulations give excellent agreement with the experimental data. Also, a simple model is put forth to explain the physical process which limits the emission of charge.

7.1. Simple model

The emission of a short pulse of electrons from the cathode can be thought of in simple terms. The maximum number of electrons which can be emitted is a function of the electric field on the cathode and the space charge field generated by the electron beam itself. For a given accelerating electric field strength there is an associated peak beam surface charge density that can be extracted, $\Sigma_m = \epsilon_0 E_z$, which is an analog, for transient beams, to the Child–Langmuir limit. To understand what is going on in our gun one must think of the local characteristics of the charge emission and take into account emission from the tails of the distribution. Because of the damage to our cathode, and the small laser spot we use, the emission is very local, with hot spots of unknown distribution and size. These local emitters attempt to exceed the maximum extractable current, and are therefore driven into saturation. However, the tails of the laser distribution are not saturated and continue to emit until they saturate as well, and so on. To this end we assume an *effective* Gaussian sigma σ_r and then calculated the emission profile as a function of charge deposited on

Table 1
Design and model parameters for the rf gun

	Design parameters	Modeled parameters
σ_τ [ps]	2	1
σ_r [mm]	3	0.3
Charge [nC]	0–3	0–3
ϕ [deg]	55	55
E_0 1/2 cell [MV/m]	100	50
E_0 full cell [MV/m]	100	100
Solenoid [A]	200	200
$\delta E/E$ [%]	0.1	3.5
$\epsilon_{x,y,n}$ [π mm mrad]	1	10
MeV/c	4.5	3.5

the cathode. We then compare the experimental data, simulation results, and theoretical curves.

7.2. Simulation

The rf gun when operating under the design parameters in Table 1 behaves as expected according to PARMELA simulations. No space charge suppression is seen, all of the charge deposited on the cathode is extracted. It has become apparent that the rf gun is not operating under its design specifications. In short, we believe that due to the damage on the cathode and the inherent laser spot size, that the effective spot sizes of photoemission are sub-millimeter. Aggravating this is the fact that it is also conceivable that the half-cell field is somewhat less than 100 MV/m. The rf gun was tuned in place to maximize its shunt impedance, but since the shunt impedance in the half cell is less per unit length than in the full cell this is not a good technique to use. To model this effect the peak field in the half cell was set to 50 MV/m and the full cell field to 100 MV/m. Also, to model the small effective emission area on the cathode an effective Gaussian spot size of $\sigma_r = 0.3$ mm was chosen. For comparison, the design parameters and the modeled parameters are given in Table 1. Fig. 1 shows the beamline configuration used. PARMELA simulations were then run with the modeled parameters from the photocathode to the first phosphor, where the extracted charge was measured. The simulation [6] was carried out from 0 to 2.3 nC in 5 pC steps. It is important to note that all of the charge that is lost is lost in the first several time steps near the cathode region showing that they are forced back into the cathode by longitudinal space charge. There are no particles lost transversely or by any other means thereafter. Fig. 2 shows a plot of the experimental quantum efficiency data and the simulated data. The experimental data was fit to a line for values below 0.5 nC and then it was extended to 2 nC. This was then plotted as a reference of what one would

expect with no space charge depleted emission. The agreement is quite good, suggesting that emission from a small damaged region coupled with a lower than expected peak rf field in the first half cell produces the observed behavior.

7.3. A simple theoretical model

Consider a radial Gaussian emission region [6] which produces a surface charge density of the form

$$\Sigma(r) = \left[\frac{Q_0}{2\pi\sigma_r^2} \right] \exp(-r^2/2\sigma_r^2), \qquad (11)$$

where σ_r is the *effective* rms spot size. Now, elementary considerations limit the maximum surface charge density which can exist before electrons are re-absorbed by the cathode to be

$$\Sigma_m = \epsilon_0 E_0 \sin(\phi_0). \qquad (12)$$

To find the total charge emitted, we must add up those emitted in this saturated region and those in the unsaturated tail. The total emitted in the saturated region is

$$Q_1 = \pi a_t^2. \qquad (13)$$

Here the saturated radius is simply

$$a_t = \sqrt{\left[2 \ln\left[\frac{Q_0}{2\pi\sigma_r^2\Sigma_m} \right] \right]}\, \sigma_r. \qquad (14)$$

We can easily integrate the charge distribution emitted in the tail,

$$Q_t = 2\pi \int_{a_t}^{\infty} \left[\frac{Q_0}{2\pi\sigma_r^2} \right] \exp(-r^2/2\sigma_r^2)r\, dr, \qquad (15)$$

which yields

$$Q_t = Q_0 \exp(-a_t^2/2\sigma_r^2). \qquad (16)$$

The total charge off the cathode is that given off in the saturated region plus that given off in the tail

$$Q_1 = \Sigma_m\pi a_t^2, \quad \text{and} \quad Q_2 = Q_0 \exp(-a_t^2/2\sigma_r^2) \qquad (17)$$

with the total

$$Q_{PS1} = Q_1 + Q_2 = Q_0 \frac{\Sigma_m}{\Sigma_0} \left[1 + \ln\left(\frac{\Sigma_0}{\Sigma_m} \right) \right], \qquad (18)$$

where

$$\Sigma_0 = \frac{Q_0}{2\pi\sigma_r^2} \qquad (19)$$

is the peak surface charge density which would be emitted without the presence of space charge forces. Note that this expression is valid only when the emission is already in saturation ($\Sigma_0 \geq \Sigma_m$). Fig. 16 shows the calculated curve plotted with the experimental data
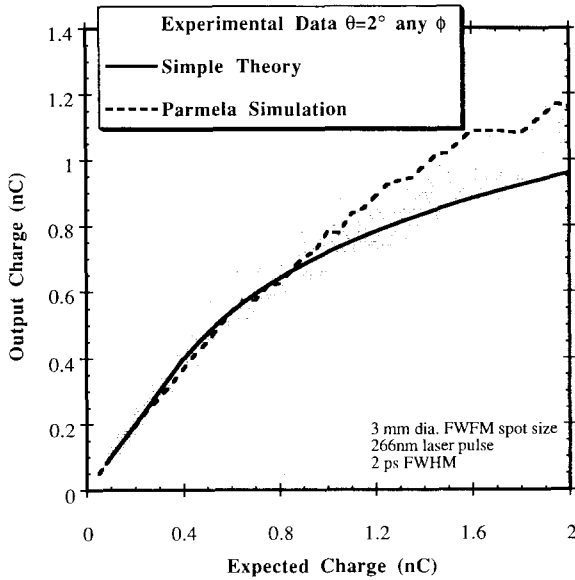
Fig. 16. Calculated curve plotted with the experimental data and PARMELA data.

Fig. 18. Length of the beam during and just after emission.

is about 0.32 mm, in close agreement with that used in the PARMELA runs.

Pulse lengthening and energy spread

and PARMELA data. The agreement is again quite good, showing that the emission is governed by the space charge saturation of the emitters, and also by the tails of the distribution. As subsequent measurements showed that the accelerating field in the half-cell was actually 67 MV/m at the laser injection time, one can actually use the data in the saturated region to deduce the emitter spot size in this model, by a single parameter fit. Fig. 17 shows a fit to the data of the ratio of emitted to expected charge. The deduced emitter size
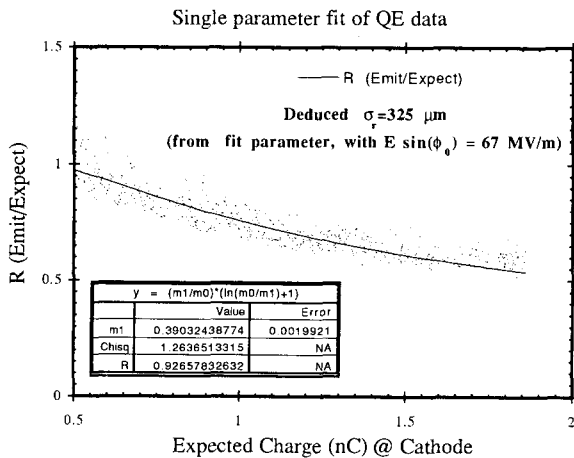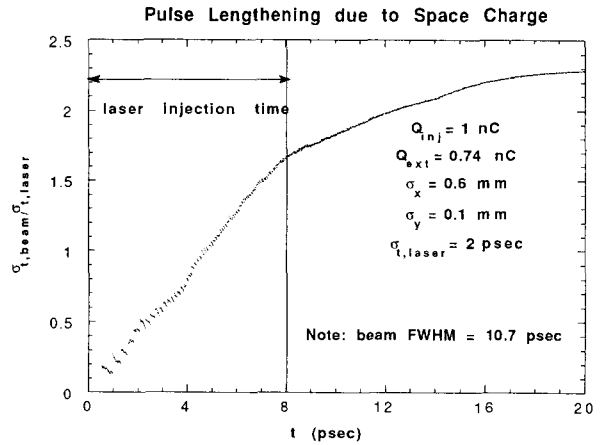
The presence of large longitudinal space charge forces which suppress the emission of the beam at the cathode obviously must also lengthen the extent in time of the beam. PARMELA was used to examine this effect. In Fig. 18, the length of the beam during and just after emission is shown, with a very fine time resolution (20 fs). The beam, which should produce a nC, only manages 0.74 nC off of the cathode, while the bunch time length expands (after only 20 ps of propagation from the beginning of the laser pulse), to 10.7 ps FWHM, from the original laser pulse length of 4.5 ps FWHM. Additional pulse lengthening due to longitudi-

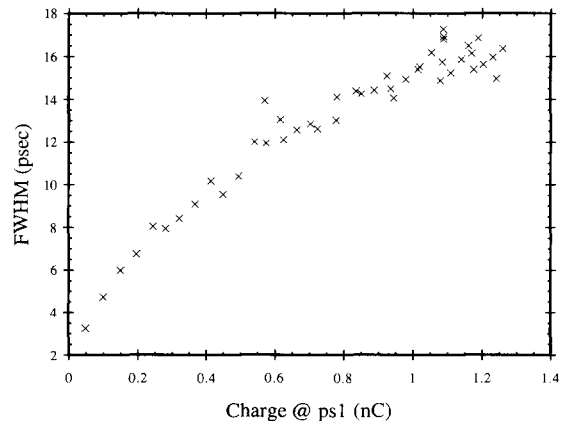Fig. 17. Ratio of emitted to expected charge.

Fig. 19. Pulse length as a function of beam charge.

nal space charge-induced energy spread, as well as beam dynamics in the solenoid, produce an even longer beam at PS1. The pulse length as a function of beam charge is shown in Fig. 19. These calculated values are in fairly good agreement with the observations.

This straightforward model of the emission from damaged areas on the cathode with tails to the distribution explain many of the curious aspects of the operation of the rf gun to date. The spot sizes quoted are all *effective* sigmas because we do not know the sigmas of the damaged regions, their numbers, or symmetries. One recommendation is that the rf gun be run at maximum rf power to obtain the highest peak accelerating field in the half-cell. The emission area is nearly fixed, due to the damage on the cathode. In the near future the rf gun should be rebalanced and a new highly polished cathode installed. One should also be extra careful not to operate the gun in the explosive emission regime (which also is aggravated by small laser spot size) or otherwise damage the cathode. The extraction of charge and ultimate propagation of the beam depends on the cathode to a high degree, so great care must be taken not to damage the cathode in any way.

8. Conclusion

The UCLA photoinjector has been operated successfully. The measurements show that the emittance scales as expected. The important thing to note is that for this set of emittance runs the rf photoinjector had a field imbalance. The field in the full cell was 1.8 times that in the half cell. This contributed to emittance blowup, as did the phosphor screens used to measure the emittance. The phosphor screens were placed onto the beamline at a 45° angle which created broadening of the line widths. The quantum efficiency measurement of Cu in a rf gun resulted in $\eta = 1 \times 10^{-4}$. The photoemission from Cu under macroscopic electric fields of 50 MV/m appears to be enhanced by damage on cathode. However, for charge levels greater than 0.25 nC the quantum efficiency is reduced by space charge near the photocathode. Despite the limitations imposed by space charge, up to 3 nC is produced from

the electron gun. For 70° laser injection, p-polarized light results in a 50% increase in quantum efficiency over s-polarized light, probably due to their relative reflectivities.

In the present experiments, the electron bunch length does not mimic the laser pulse length. The shortest Cerenkov streak measurements indicate 9 ps bunch lengths. The physical mechanism for this bunch lengthening is under investigation. PARMELA simulations showed that bunch lengthening on the order of 10 ps can occur due to space charge, although the bunch length measurements did not show a correlation between bunch length and charge output from the gun. However, even with the bunch lengthening, beam currents of 100 A are produced.

References

[1] S.C. Hartman et al., Particle Accelerator Conf., San Francisco, CA, 1991, p. 2967.
[2] K. Batchelor et al., European Particle Accelerator Conf., Rome, Italy, June 7–12, 1988.
[3] C. Pellegrini et al., Particle Accelerator Conf., Washington, DC, 1993.
[4] Handbook of Chemistry and Physics.
[5] K.-J. Kim, Nucl. Instr. and Meth. A 275 (1989) 201.
[6] S.C. Hartman and J.B. Rosenzweig, UCLA-CAA-TECH-NOTE-internal, 1993.
[7] S.C. Hartman et al., Particle Accelerator Conf., Washington, DC, 1993.
[8] C. Lejeune and J. Aubert (eds.), Emittance and Brightness Definitions and Measurements (Academic Press, New York, 1980).
[9] G. Hairapetian et al., Particle Accelerator Conf., Washington, DC, 1993.
[10] K.T. McDonald, IEEE Trans. Electron Devices ED-35 (1988) 2052.
[11] J. Davis et al., Particle Accelerator Conf., Washington, DC, 1993.
[12] D.W. Decker, J.P. Waldron and R.J. Jaccodine, J. Opt. Soc. Am. 54 (1964) 216.
[13] Y. Kawamura and K. Toyoda, Appl. Phys. Lett. 45 (1984) 307.
[14] Appl. Phys. Lett. 49 (1986) 912.
[15] T. Srinivasan-Rao, J. Ficher and T. Tsang, J. Appl. Phys. 69 (1991) 3291.